nature structural & molecular biology

Molecular basis of caspase-1 polymerization and its inhibition by a new capping mechanism

Alvin Lu[1,2,9], Yang Li[1,2,9], Florian I Schmidt[3], Qian Yin[1,2,8], Shuobing Chen[4,5], Tian-Min Fu[1,2], Alexander B Tong[1,2], Hidde L Ploegh[3,6], Youdong Mao[4,5,7] & Hao Wu[1,2]

Inflammasomes are cytosolic caspase-1-activation complexes that sense intrinsic and extrinsic danger signals, and trigger inflammatory responses and pyroptotic cell death. Homotypic interactions among Pyrin domains and caspase recruitment domains (CARDs) in inflammasome-complex components mediate oligomerization into filamentous assemblies. Several cytosolic proteins consisting of only interaction domains exert inhibitory effects on inflammasome assembly. In this study, we determined the structure of the human caspase-1 CARD domain (caspase-1^{CARD}) filament by cryo-electron microscopy and investigated the biophysical properties of two caspase-1-like CARD-only proteins: human inhibitor of CARD (INCA or CARD17) and ICEBERG (CARD18). Our results reveal that INCA caps caspase-1 filaments, thereby exerting potent inhibition with low-nanomolar K_i on caspase-1^{CARD} polymerization *in vitro* and inflammasome activation in cells. Whereas caspase-1^{CARD} uses six complementary surfaces of three types for filament assembly, INCA is defective in two of the six interfaces and thus terminates the caspase-1 filament.

As a first line of defense, supramolecular assemblies known as inflammasomes activate inflammatory caspases including caspase-1, caspase-11 (mouse), and caspase-4 and caspase-5 (human) in response to pathogenic invasion and cellular perturbation[1,2]. Absent in melanoma 2 (AIM2)-like receptors and proteins containing nucleotide-binding domains and leucine-rich-repeats (NLRs) are inflammasome sensors that respond to a variety of pathogen-associated molecular patterns (including cytosolic double-stranded DNA and bacterial flagellin) as well as danger-associated molecular patterns (such as extracellular ATP, uric acid crystals, and reactive oxygen species)[3]. AIM2-like receptors and most NLRs contain a Pyrin domain (PYD), which recruits apoptosis-associated speck-like protein containing a CARD (ASC) through PYD-PYD interactions. ASC also possesses a CARD and links the PYD-containing sensor proteins to caspase recruitment, dimerization, and autoproteolytic activation through CARD-CARD interactions. Both PYD and CARD belong to the death domain (DD)-fold superfamily, which is characterized by a conserved six-helix bundle fold[4], and interact through nucleated polymerization and filament formation[5,6]. The NLR family proteins NLRBs (also known as NAIPs) do not contain a PYD or CARD and signal through the CARD-containing NLRC4 adaptor[7,8], which similarly recruits caspase-1 through CARD-CARD interactions[7,9,10]. Activated caspases proteolytically process pro-IL-1β and pro-IL-18. The mature cytokines, once released, initiate downstream signaling events leading to the transcription of many proinflammatory and antiviral genes[11]. Inflammatory caspase activation can also lead to pyroptotic cell death characterized by spillage of cellular contents.

CARD-CARD interactions are essential for the assembly of all inflammasomes. Therefore, it is not surprising that a number of CARD-only proteins (COPs) inhibit inflammasome formation and cytokine maturation[12–18]. Regulation by COPs has been proposed to arise because of selective pressure and a need for higher tolerance for inflammatory stimuli. Interestingly, rodents and primates all have caspase-1, but COPs are found only in higher primates, thus suggesting that these genes must have emerged after the human–mouse divergence[18]. The genes of proposed CARD-only inhibitors, COP1 (also known as Pseudo-ICE and CARD16), INCA (also known as CARD17), and ICEBERG (also known as CARD18), reside near the caspase-1 locus, as a result of a series of gene duplication events[19]. New stop codons have led to transcripts missing several downstream exons, thus resulting in the translation of CARDs lacking the caspase domain[20,21]. INCA and ICEBERG share 83% and 53% identity, respectively, with caspase-1 CARD, and they may have evolved new mechanisms in their functions. Additionally, INCA and caspase-1 are simultaneously upregulated by IFN-γ in the human monocytic cell lines THP-1 and U937, and ICEBERG, but not INCA, is induced by lipopolysaccharide (LPS) and the cytokine TNFα[15,16]. Therefore, INCA and ICEBERG may play distinct roles in different biological settings.

[1]Department of Biological Chemistry and Molecular Pharmacology, Harvard Medical School, Boston, Massachusetts, USA. [2]Program in Cellular and Molecular Medicine, Boston Children's Hospital, Boston, Massachusetts, USA. [3]Whitehead Institute for Biomedical Research, Cambridge, Massachusetts, USA. [4]Center for Quantitative Biology, Peking-Tsinghua Joint Center for Life Sciences, Academy for Advanced Interdisciplinary Studies, State Key Laboratory for Artificial Microstructures and Mesoscopic Physics, School of Physics, Peking University, Beijing, China. [5]Department of Cancer Immunology and Virology, Intel Parallel Computing Center for Structural Biology, Dana-Farber Cancer Institute, Boston, Massachusetts, USA. [6]Department of Biology, Massachusetts Institute of Technology, Cambridge, Massachusetts, USA. [7]Department of Microbiology and Immunobiology, Harvard Medical School, Boston, Massachusetts, USA. [8]Present address: Department of Biological Science, Florida State University, Tallahassee, Florida, USA. [9]These authors contributed equally to this work. Correspondence should be addressed to H.W. (wu@crystal.harvard.edu).

Received 8 November 2015; accepted 10 March 2016; published online 4 April 2016; doi:10.1038/nsmb.3199

To fill the knowledge gap on inflammasome activation by CARD-CARD interactions, we determined the caspase-1^{CARD} filament structure through cryo-EM and performed detailed biochemical analyses to elucidate the mechanisms of inhibition by INCA and ICEBERG. Our results provide what is, to our knowledge, the first glimpse of a CARD complex in the pathway and further demonstrate differential functional effects of ICEBERG and INCA. ICEBERG nucleates the formation of caspase-1 filaments and is incorporated into caspase-1 filaments, but it cannot effectively inhibit inflammasome activation. As previously suggested, ICEBERG may function by interfering with the interaction between caspase-1 and other CARD-containing proteins[17]. Here, we found that, unexpectedly, in contrast to ICEBERG, INCA at low-nanomolar concentrations capped caspase-1^{CARD} oligomers, thus preventing their polymerization and robustly inhibiting inflammasome assembly *in vitro*. Moreover, induced expression of INCA in the THP-1 cell line strongly inhibited inflammasome activation. Collectively, our study expands the structural knowledge on CARD-CARD interactions during inflammasome assembly and regulation.

RESULTS

Cryo-EM reconstruction of the caspase-1^{CARD} filament

We generated a histidine- and maltose-binding protein (His-MBP)-tagged (termed sandwich-tagged) caspase-1^{CARD}-SUMO fusion construct designed to disrupt caspase-1^{CARD} self-oligomerization during overexpression in *Escherichia coli* (**Fig. 1a**). We purified the fusion protein as a monomer by size-exclusion chromatography. After removal of the N-terminal His-MBP tag by the tobacco etch virus (TEV) protease, extended individual filaments of several hundred nanometers in length spontaneously formed, as detected in cryo-electron micrographs (**Fig. 1b**). An average power spectrum revealed visible layer lines resembling those of the MAVS^{CARD} filament in the RIG-I pathway[22], despite the lack of a meridional layer line (**Fig. 1c** and **Supplementary Fig. 1a**). Assuming close similarity among these filaments, we derived a calculated initial one-start helical symmetry of −100.23° and 5.06 Å in rotation and rise per subunit, respectively (**Fig. 1c**). Beginning from a solid cylinder model and using iterative helical real-space reconstruction (IHRSR)[23], we obtained a final volume containing mostly α-helices with refined helical parameters of −100.21° and 5.10 Å (**Fig. 1d**). We were readily able to position a homology structure model of caspase-1^{CARD} that we derived from the NMR structure of ICEBERG[16] into the density, thus indicating the correctness of the reconstruction (**Fig. 1d** and **Supplementary Fig. 1b**,**c**). The reconstructed volume also displayed disordered density outside the caspase-1^{CARD} filament core; this density may correspond to the flexible C-terminal SUMO tag (**Fig. 1d**). Using both gold-standard and model-versus-map Fourier-shell-correlation plots, we generated a reconstruction of ~4.8-Å resolution, with resolved density for some large side chains (**Supplementary Fig. 1b–e**), including many at the interface (described below). The final caspase-1^{CARD} model was highly similar to the ICEBERG structure (**Supplementary Fig. 1f**,**g**).

Structure of the caspase-1^{CARD} filament

The caspase-1^{CARD} filament had an approximate diameter of 8 nm and an inner hole of <1 nm (**Fig. 2a**). On the basis of an extended conformation of the ~39-residue linker between the CARD and the caspase domains in caspase-1, the closely packed caspase-1^{CARD} in the filament would bring the local concentration of the caspase domain to ~3.1 mM. The caspase-1^{CARD} filament forms a left-handed one-start helical assembly consisting of approximately four subunits per turn, a configuration similar to that of the Myddosome DD complex and the MAVS^{CARD} filament[22,24], on the basis of the three previously defined types of asymmetric interactions[4,25] (**Fig. 2b**). The type III interface exhibits interactions in the helical-strand direction. The type I and type II interfaces provide interaction between the helical turns (**Fig. 2c**). The type I interface is the most extensive of the three types, with electrostatic complementarity (**Fig. 2d**). Because of the potential inaccuracies in side chain conformations at this resolution, we describe the type Ia patch as collectively involving residues in helices α1 and α4 (such as K11, R10, R15, R55, and D52), which interact with residues in helix α2 (such as Q31, E28, D27, and N23) (**Fig. 2e**). In contrast, the type II interaction requires an exposed hydrophobic residue, Y82 in the α5–α6 loop of one subunit, to be inserted into the α2–α3 loop of the adjacent subunit (**Fig. 2f**). The type III interface appears to be the least extensive and may contribute less binding energy during filament formation (**Fig. 2g**).

To validate the importance of these interfacial residues, we generated site-directed mutants and compared their properties with those of wild-type (WT) caspase-1^{CARD} (**Fig. 2h**,**i**). We used GFP-tagged caspase-1^{CARD} for these experiments because the fusion protein primarily formed soluble short filaments, similarly to the GFP-AIM2^{PYD} protein[26]. We first analyzed whether the mutations reduced the aggregation tendency of GFP-tagged

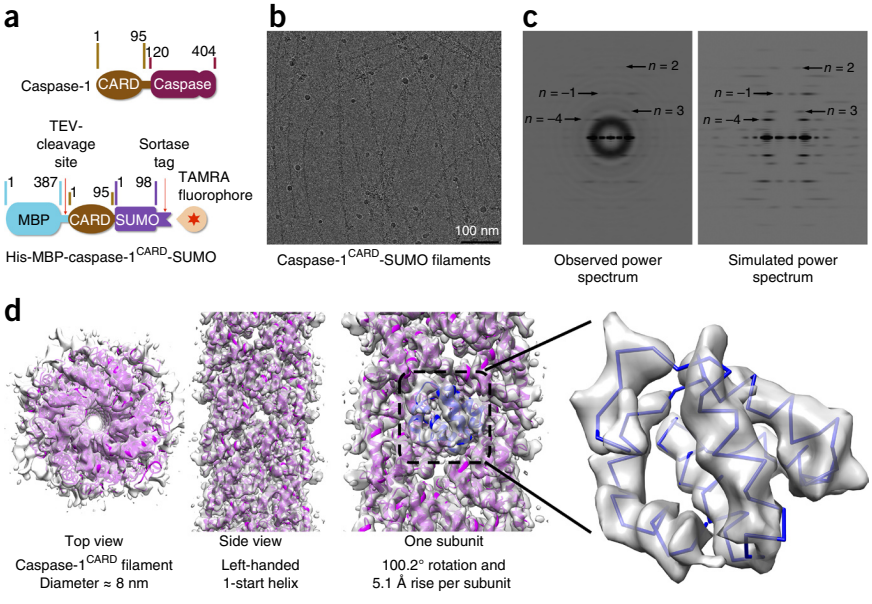

Figure 1 Cryo-EM structure determination of the caspase-1^{CARD} filament. (**a**) Domain organization of pro-caspase-1 and its CARD construct for reconstruction and *in vitro* fluorescence polarization assay. (**b**) A representative cryo-EM image (from a total of 509 video-mode micrographs collected). (**c**) Close agreement between experimental and simulated power spectra. Selective layer lines (*n*) are labeled. (**d**) Reconstructed cryo-EM map fitted with the caspase-1^{CARD} model in magenta with one subunit highlighted in blue. At right, cryo-EM density is shown in zoom view and is superimposed with a fitted caspase-1^{CARD} molecule.

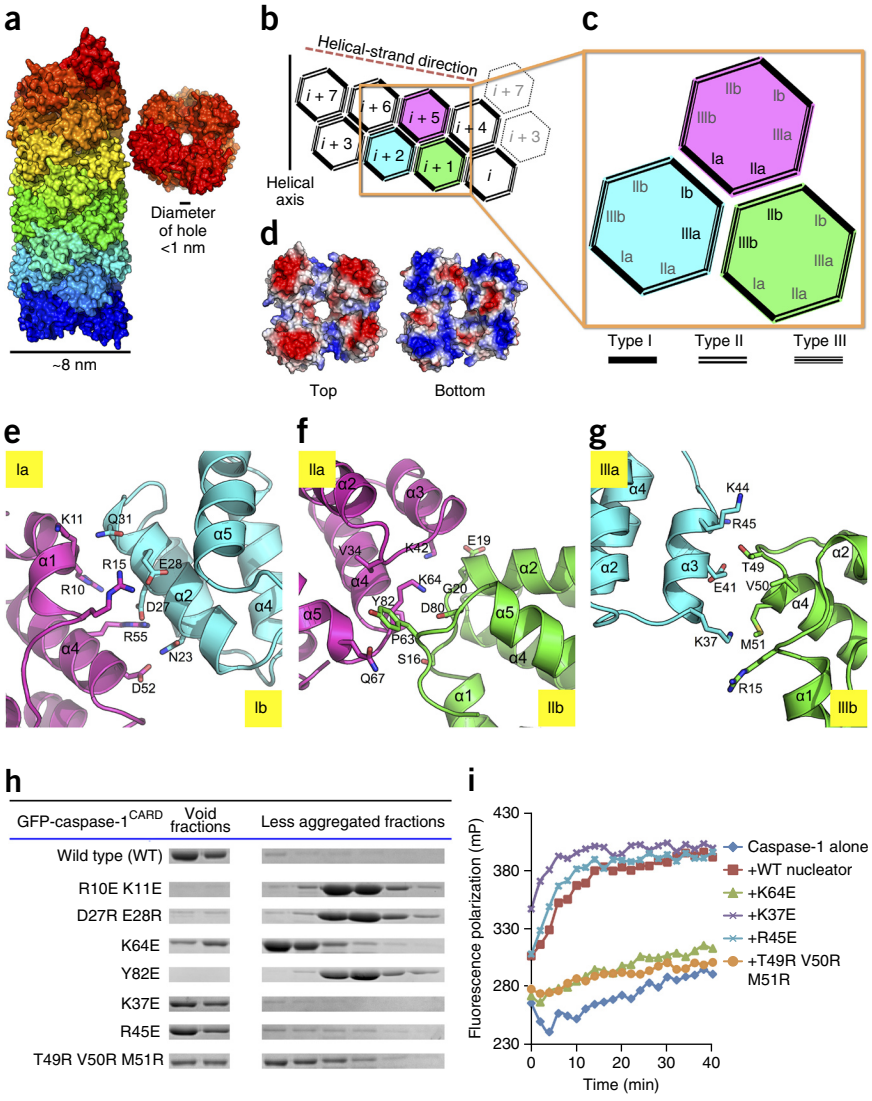

Figure 2 Structural analysis of the caspase-1^{CARD} filament. (**a**) Surface representation of the caspase-1^{CARD} filament structure. Different subunits are shaded with colors from red to violet. (**b**) Schematic diagram of the helical filament, with three neighboring subunits highlighted in magenta, green, and cyan. (**c**) Relative orientations of the type Ia, Ib, IIa, IIb, IIIa, and IIIb patches. (**d**) Electrostatic-surface renderings of a tetrameric turn, showing complementary charges. (**e**–**g**) The type I (**e**), type II (**f**), and type III (**g**) interfaces. Given the current resolution, the precise side chain conformations are not implied in the representation. (**h**) Size-exclusion chromatography analysis showing void and soluble fractions of WT and mutant capsase-1^{CARD}. Original images of gels can be found in **Supplementary Data Set 1**. (**i**) Assay of void fractions of WT and mutants for their ability to nucleate monomeric WT caspase-1^{CARD} to form filaments. Approximately 140 nM of each nucleator sample and TEV protease were added to 4 μM of TAMRA-labeled His-MBP-caspase-1^{CARD}-SUMO for polymerization. Source Data for **i** are available online.

caspase-1^{CARD} by using size-exclusion chromatography. We then determined whether the mutations decreased the ability of GFP-tagged caspase-1^{CARD} to promote filament formation of WT monomeric caspase-1^{CARD} by using fluorescence polarization (FP). For the second experiment, we added a C-terminal sortase motif to the His-MBP-caspase-1^{CARD}-SUMO construct used for cryo-EM. We labeled the fusion protein with the fluorophore TAMRA with recombinant sortase A[27] (**Fig. 1a**) and initiated caspase-1^{CARD} polymerization by removal of the His-MBP tag by the TEV protease. WT GFP-caspase-1^{CARD}, which formed short filaments[5], robustly nucleated caspase-1^{CARD} polymerization, as indicated by increased FP values (**Supplementary Fig. 2**). The apparent nucleation potency of WT GFP-caspase-1^{CARD} was ~283.0 ± 1.4 nM (**Supplementary Fig. 2**).

Whereas GFP-tagged WT caspase-1^{CARD} eluted exclusively in the void volume of a Superdex 200 gel-filtration column, charge-reversal mutations at the type Ia (R10E K11E) and Ib (D27R E28R) patches abolished formation of caspase-1^{CARD} filaments, thus reflecting the importance of electrostatic interactions at the type I interface (**Fig. 2h**). The Y82E mutation at the type IIb patch also completely abolished filament formation. In contrast, the charge-reversal mutation at the type IIa patch, K64E, only impaired but did not abrogate filament formation, thus suggesting that the type II interface is probably contributed predominately by hydrophobic interactions. In the caspase-1^{CARD} polymerization assay, K64E was completely incapable of nucleating WT caspase-1^{CARD} filament formation (**Fig. 2i**). Charge-reversal mutations at the type IIIa patch (K37E or R45E) did not affect either filament formation or nucleation. Only a triple mutation (T49R V50R M51R) at the type IIIb surface impaired aggregation and nucleation potency (**Fig. 2h**,**i**), consistently with less extensive of type III interactions. These results strongly correlated with our analysis of the caspase-1^{CARD} cryo-EM structure.

Caspase-1^{CARD} filament versus other DD complexes

We compared the structure of the caspase-1^{CARD} filament to the structures of other existing DD-fold complexes by pairwise structural alignment between isolated dimers of caspase-1^{CARD} and dimers of other DD-fold complexes. Within the CARD subfamily, $MAVS^{CARD}$ is the only other high-resolution filament structure recently determined by cryo-EM. Although both domains have very low sequence identity, the helical parameters of $MAVS^{CARD}$ and caspase-1^{CARD} are similar, perhaps owing to the relative location of the interfaces (**Supplementary Fig. 3a**–**c**). We also compared the buried residues with respect to each type of interaction and found that the relative location of these residues indeed correlated very well between the two CARDs (**Supplementary Fig. 3d**). For a quantitative comparison, we aligned one subunit of each interface type and measured how much rotation was required to overlap the other subunit (**Supplementary Fig. 3e**). Between $MAVS^{CARD}$ and caspase-1^{CARD}, the rotations for type I, II, and III were 10.2°, 8.1°, and 14.1°, respectively. Between caspase-1^{CARD} and $MyD88^{DD}$, the

respective rotations were 14.1°, 8.3°, and 13.3°, and between caspase-1^{CARD} and RAIDD^{DD}, the respective rotations were 10.6°, 11.3°, and 21.8°, thus indicating the more dissimilar quaternary structures. Overall, these angular differences were smaller than the relative rotations between interactions in the caspase-1^{CARD} filament and the ASC^{PYD} filament (14.8°, 32.5°, and 42.3° for types I–III, respectively). This phenomenon may be partially attributed to the helical parameters of the oligomeric structures. The caspase-1^{CARD} filament, MAVS^{CARD} filament, and the Myddosome are all left-handed one-start helical assemblies, whereas the ASC^{PYD} filament is a right-handed three-start helical assembly[5].

INCA displays properties distinct from those of caspase-1 and ICEBERG

We expressed histidine-tagged human INCA and ICEBERG, and found that whereas INCA was soluble and monomeric, ICEBERG was largely insoluble (**Fig. 3a**,**b**). To investigate the biochemical properties of ICEBERG, we fused it to the C terminus of His-MBP to increase its solubility. His-MBP-ICEBERG was soluble but eluted in the void volume of a Superdex 200 size-exclusion column. Removal of the His-MBP tag resulted in the formation of long and bundled filaments, as shown by negative-stain EM (**Fig. 3c**). The NMR structure of ICEBERG solved at pH 3.8, under which the protein is monomeric[16], shows a typical CARD structure with a six-helix bundle fold highly similar to that of ASC^{CARD} (ref. 28). INCA shares similar predicted secondary structures and 55% sequence identity with ICEBERG with no gaps in the alignment, thus suggesting that INCA may have a structure highly similar to that of ICEBERG (**Fig. 3d**). However, ICEBERG and INCA have contrasting biophysical properties in solution. Because sequence comparisons revealed identities of 53% for ICEBERG and caspase-1^{CARD}, and 83% for INCA and caspase-1^{CARD} (**Fig. 3d**), it is therefore the less homologous ICEBERG that has a filament-forming ability similar to that of caspase-1^{CARD}, whereas INCA is monomeric.

ICEBERG promotes and INCA inhibits formation of caspase-1^{CARD} filaments

We used the caspase-1^{CARD} polymerization assay to probe the effects of the COPs on caspase-1 polymerization. After removal of the His-MBP tag by addition of TEV protease, caspase-1^{CARD}-SUMO formed filaments at a negligibly slow rate, as shown by the minimal change in FP (**Fig. 4a**). ICEBERG greatly enhanced formation of caspase-1^{CARD} filaments, thus suggesting that oligomeric ICEBERG provided seeds for polymerization of monomeric caspase-1^{CARD}. In contrast, addition of INCA did not have substantial effects on caspase-1^{CARD} filament formation at its low basal rate.

In ASC-dependent inflammasomes, the CARD of the adaptor ASC nucleates caspase-1^{CARD} polymerization[5]. To recapitulate this scenario *in vitro*, we expressed His-GFP fused to ASC^{CARD}, the majority of which eluted in the void volume of a Superdex 200 size-exclusion column (**Fig. 4b**). Negative-stain EM indicated that the protein formed short His-GFP-ASC^{CARD} filaments (**Fig. 4c**). Addition of these ASC^{CARD} filaments at levels well below stoichiometry robustly potentiated caspase-1^{CARD} polymerization, with an apparent dissociation constant (K_{app}) of 108.0 ± 1.4 nM (**Fig. 4d**). Using fixed His-GFP-ASC^{CARD} and caspase-1^{CARD} concentrations, we added substoichiometric amounts of INCA and measured the rates of filament formation. Notably, very low concentrations of INCA were sufficient to substantially inhibit caspase-1^{CARD} filament formation (**Fig. 4e**). The apparent inhibitory constant (K_i) was 9.4 ± 1.4 nM (**Fig. 4e**).

To address the question of whether ICEBERG interacts with ASC^{CARD}, we designed an ASC^{CARD} polymerization assay similar to the caspase-1^{CARD} assay. We expressed and purified monomeric His-MBP-ASC^{CARD}-SUMO with a C-terminal sortase motif and

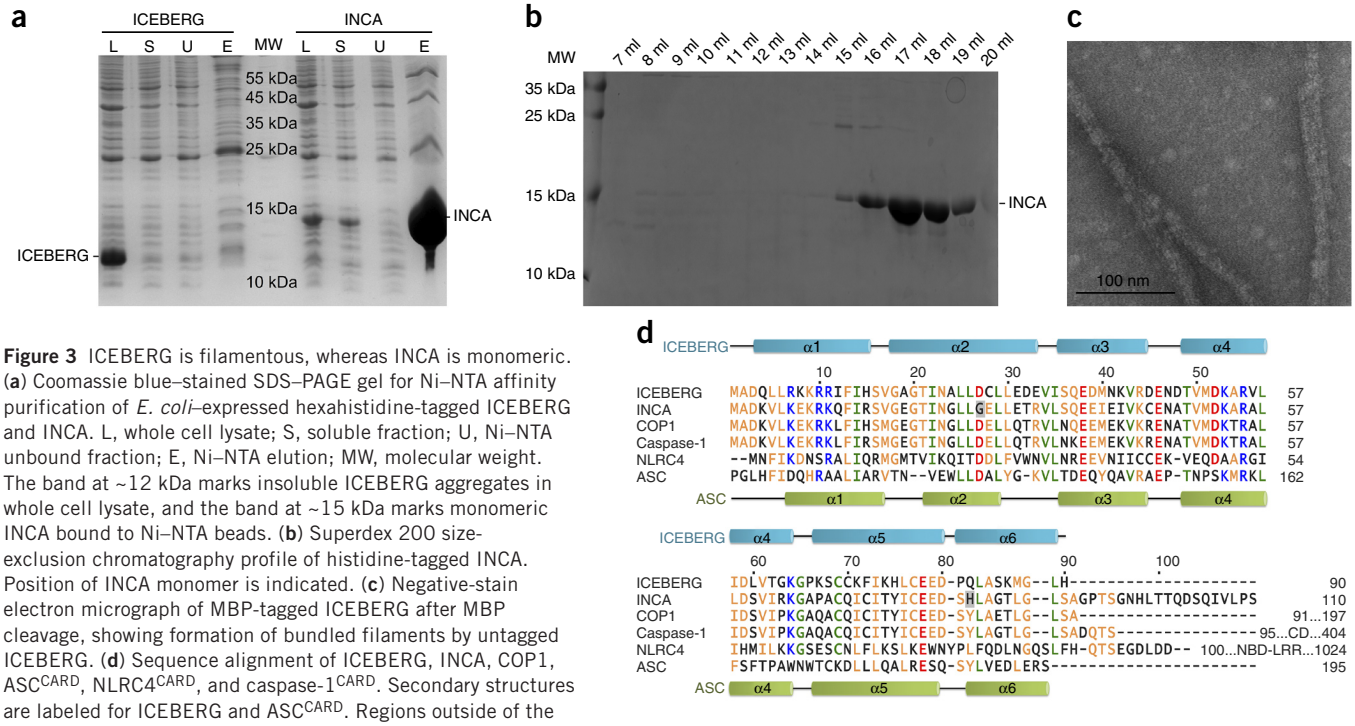

Figure 3 ICEBERG is filamentous, whereas INCA is monomeric. (**a**) Coomassie blue–stained SDS–PAGE gel for Ni–NTA affinity purification of *E. coli*–expressed hexahistidine-tagged ICEBERG and INCA. L, whole cell lysate; S, soluble fraction; U, Ni–NTA unbound fraction; E, Ni–NTA elution; MW, molecular weight. The band at ~12 kDa marks insoluble ICEBERG aggregates in whole cell lysate, and the band at ~15 kDa marks monomeric INCA bound to Ni–NTA beads. (**b**) Superdex 200 size-exclusion chromatography profile of histidine-tagged INCA. Position of INCA monomer is indicated. (**c**) Negative-stain electron micrograph of MBP-tagged ICEBERG after MBP cleavage, showing formation of bundled filaments by untagged ICEBERG. (**d**) Sequence alignment of ICEBERG, INCA, COP1, ASC^{CARD}, NLRC4^{CARD}, and caspase-1^{CARD}. Secondary structures are labeled for ICEBERG and ASC^{CARD}. Regions outside of the aligned CARDs are indicated by residue numbers at the end of the alignment. Caspase-1 has a caspase domain (CD) ending with residue 404. COP-1 has a C-terminal region spanning ~100 residues with an unknown fold. NLRC4 has a nucleotide-binding domain (NBD) followed by leucine-rich repeats (LRR), which ends at residue 1024.

labeled the protein with the TAMRA fluorophore *in vitro*, using recombinant sortase A. Upon addition of the TEV protease, filamentous His-GFP-ASC^{CARD} acted as a nucleator in polymerization of the labeled, His-MBP-removed monomeric ASC^{CARD}-SUMO, as indicated by increasing FP as a function of time. In contrast, ICEBERG did not promote ASC^{CARD} filament formation (**Supplementary Fig. 4a**). Moreover, ICEBERG did not inhibit His-GFP-ASC^{CARD}-nucleated ASC^{CARD} polymerization (**Supplementary Fig. 4b**). Hence, we conclude that there is no apparent interaction between ICEBERG and ASC^{CARD}.

INCA directly inhibits caspase-1 polymerization

The inhibitory effect of INCA with low-nanomolar potency in ASC^{CARD}-induced caspase-1^{CARD} polymerization was remarkable. To determine whether INCA directly interacts with ASC or caspase-1, we coexpressed the proteins in pairs. We cloned INCA into the pDW363 vector with an N-terminally fused biotin-acceptor peptide (BAP), which allows biotinylation in *E. coli* by the biotin ligase BirA expressed from the same vector[29]. We first coexpressed biotinylated INCA with His-GFP-ASC^{CARD}. Ni–NTA affinity purification and gel-filtration chromatography yielded strong Coomassie blue–stained bands of His-GFP-ASC^{CARD} but no bands of copurified INCA (**Fig. 5a**). Streptavidin western blotting revealed a weak band of biotinylated INCA that copurified with His-GFP-ASC^{CARD} (**Fig. 5a**). To clarify whether this apparent weak interaction has any functional importance, we assessed the ability of INCA to inhibit this process in the ASC^{CARD} polymerization assay. Suprastoichiometric amounts of INCA, at up to 10 μM, did not inhibit His-GFP-ASC^{CARD}-nucleated ASC^{CARD} filament formation (**Fig. 5b**), thus suggesting that the ASC^{CARD}-INCA interaction does not exert any functional effect.

To determine whether INCA interacts with caspase-1^{CARD}, we coexpressed the BAP-INCA fusion with His-GFP-caspase-1^{CARD}. Unlike His-GFP-ASC^{CARD}, His-GFP-caspase-1^{CARD} copurified with sufficient amounts of INCA to be visible on Coomassie blue–stained SDS–PAGE at 7 and 8 ml (**Fig. 5c**). Streptavidin western blotting further confirmed that the bands were biotinylated INCA, thus demonstrating a direct interaction between INCA and caspase-1^{CARD}. CARD domains of both ASC and caspase-1 were present in the assays that we used to demonstrate inhibition of caspase-1 polymerization by INCA (**Fig. 4e**). The assay was thus not suitable to determine whether INCA acts on CARD domains of ASC or caspase-1. We therefore performed an alternative experiment using His-GFP-caspase-1^{CARD} as the nucleator. As described above, His-GFP-caspase-1^{CARD} and His-GFP-ASC^{CARD} were similarly potent in nucleating monomeric caspase-1^{CARD} into extended filaments (**Fig. 4d** and **Supplementary Fig. 2**). Addition of INCA at very low concentrations dramatically inhibited His-GFP-caspase-1^{CARD}-induced caspase-1^{CARD} polymerization (**Fig. 5d**). The K_i was 4.3 ± 1.4 nM, a value similar to that obtained in His-GFP-ASC^{CARD}-induced caspase-1^{CARD} polymerization (**Fig. 4e**). We also subjected the His-GFP-caspase-1^{CARD}–biotinylated INCA complex (**Fig. 5c**) to streptavidin–gold and Ni–NTA–gold labeling and observed that INCA localized exclusively at the tip of caspase-1^{CARD} filaments (**Fig. 5e**,**f**).

The concentrations of monomeric caspase-1^{CARD} and the preformed filamentous nucleators used in the polymerization assays were 4.0 μM and 0.1 μM, respectively. Intriguingly, INCA inhibited the polymerization reactions with low-nanomolar K_i, which was approximately three orders of magnitude lower than the concentration of monomeric caspase-1 and approximately one-tenth to one-twenty-fifth of concentrations of the filamentous nucleators. Therefore, a plausible explanation might be that INCA interacts with

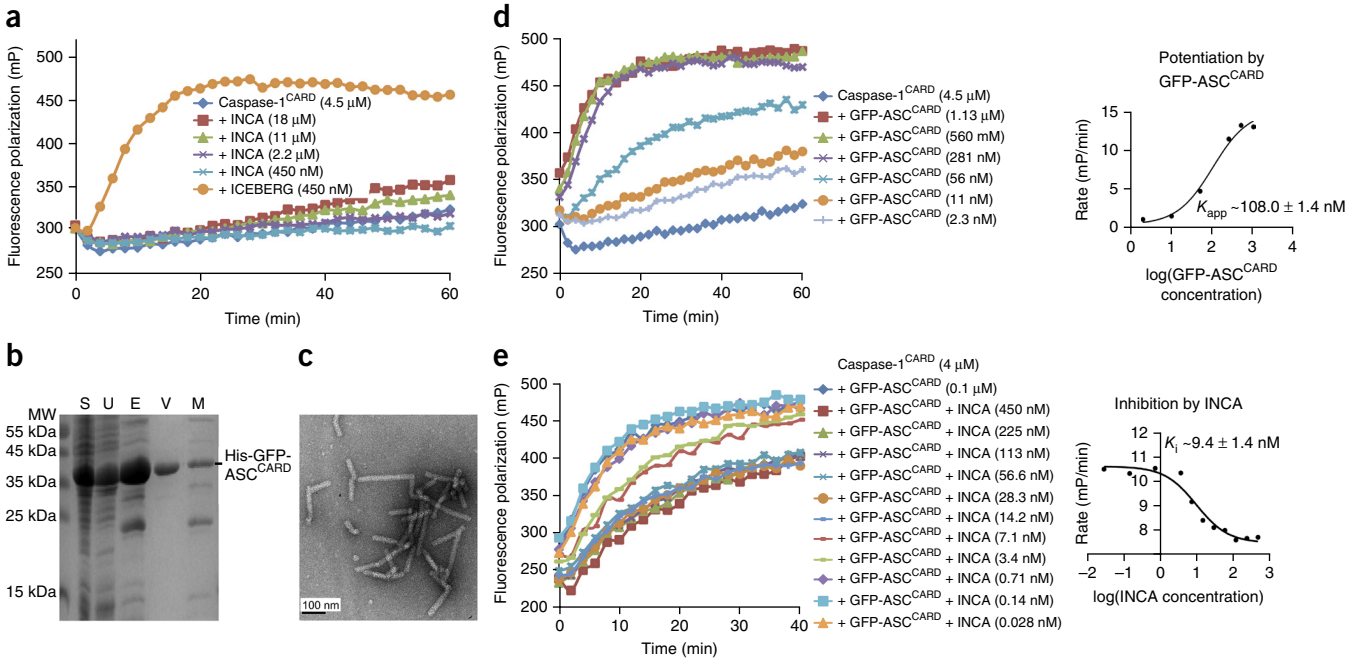

Figure 4 INCA inhibits ASC^{CARD}-nucleated formation of caspase-1^{CARD} filaments. (**a**) Nucleation of caspase-1^{CARD} filament formation by ICEBERG but not INCA. Data are an average of triplicate experiments. (**b**) Ni–NTA affinity purification and size-exclusion chromatography of His-GFP-tagged ASC^{CARD}. S, soluble fraction of bacterial lysate; U, Ni–NTA unbound fraction; E, Ni–NTA elution; V, void fraction; M, monomer fraction in gel filtration. (**c**) Negative-stain electron micrograph of the His-GFP-ASC^{CARD} void fraction. (**d**) Nucleation effects of GFP-tagged ASC^{CARD} at different concentrations on caspase-1^{CARD} filament polymerization. Calculated K_{app} (with fitting error) is shown at right. (**e**) Inhibitory effects of INCA at different concentrations on His-GFP-ASC^{CARD}-nucleated caspase-1^{CARD} filament formation. Calculated K_i (with fitting error) is shown at right. Source data for **a**, **d** and **e** are available online.

only the filamentous form of caspase-1. This interaction directly occurred on the His-GFP-caspase-1^{CARD} filaments. When we used His-GFP-ASC^{CARD} filaments, monomeric caspase-1 polymerized on these nucleators. Then His-GFP-ASC^{CARD}–caspase-1^{CARD} complex filaments became able to directly interact with INCA. It is conceivable that in both cases, the nucleators were capped with INCA, thus leading to inhibition of polymerization.

On the basis of the gold-labeling experiment (**Fig. 5e**,**f**), we quantitatively estimated this strength of inhibition by capping. The average length of the His-GFP-caspase-1^{CARD} filaments was ~150 nm, on the basis of the electron micrographs. We derived a similar length estimate for His-GFP-ASC^{CARD} filaments (**Fig. 4c**). Given the observed axial rise per subunit of 5.1 Å for the caspase-1^{CARD} filament, the total number of subunits per filament was ~30 (**Fig. 1d**). This result suggests that the effective concentration of His-GFP-caspase-1^{CARD} nucleator would be ~30-fold lower, approximately 3 nM, a value in the same order of magnitude as the K_i of INCA inhibition. Collectively, these data are consistent with the conclusion that INCA inhibits

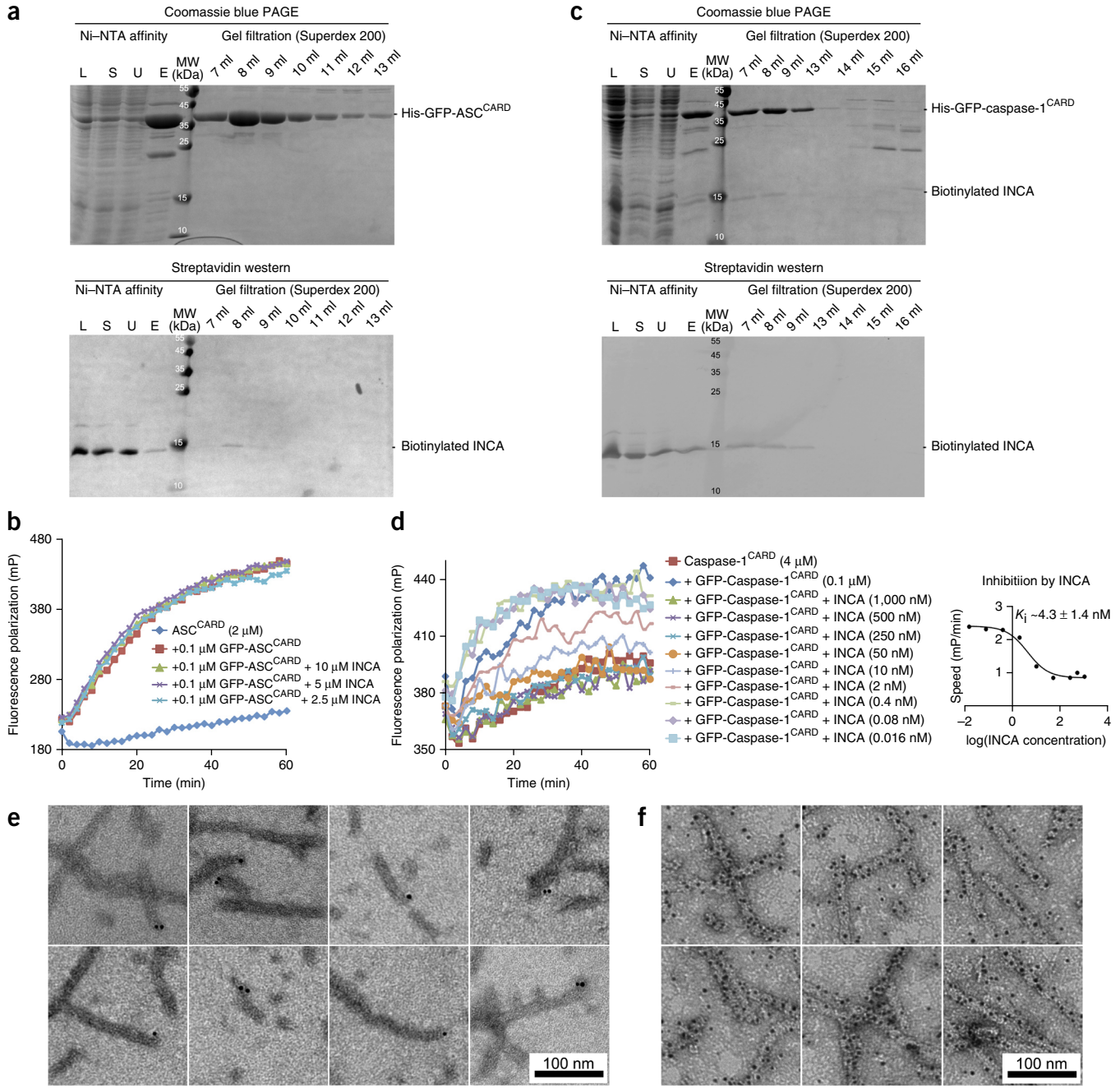

Figure 5 INCA preferentially interacts with caspase-1^{CARD}. (**a**) Western blot showing no significant interaction between co-expressed His-GFP-ASC^{CARD} and biotinylated INCA. (**b**) FP assay showing failure of suprastoichiometric amounts of INCA to inhibit His-GFP-ASC^{CARD}-nucleated ASC^{CARD} filament formation. Averages of triplicate experiments are plotted. (**c**) PAGE gel showing interaction between co-expressed His-GFP-caspase-1^{CARD} and biotinylated INCA. (**d**) FP assay showing that substoichiometric amounts of INCA inhibit His-GFP-caspase-1^{CARD}-nucleated caspase-1^{CARD} filament formation. Averages of duplicate experiments are plotted, and K_i with fitting error is shown. (**e**,**f**) Negative-stain electron micrographs of the complex (as shown in **c** at 7 ml) between His-GFP-caspase-1^{CARD} and biotinylated INCA after streptavidin–gold labeling (**e**) or Ni–NTA–gold labeling (**f**). Source data for **b** and **d** are available online.

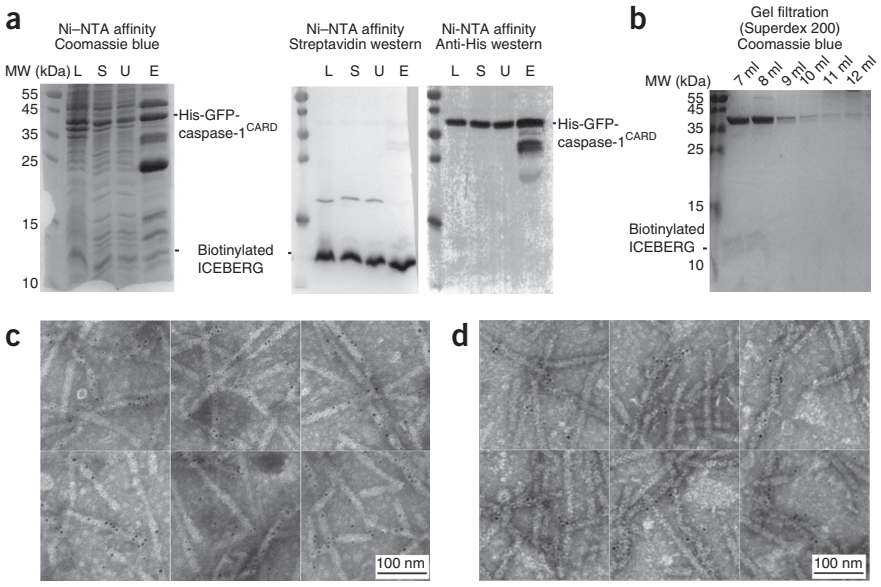

Figure 6 ICEBERG interacts with caspase-1^{CARD} by comixing. (**a**) SDS–PAGE and Western blots confirming the presence of ICEBERG in complex with His-GFP-caspase-1^{CARD} after Ni–NTA affinity chromatography. Samples are from cells coexpressing His-GFP-caspase-1^{CARD} and biotinylated ICEBERG. L, whole cell lysate; S, soluble fraction; U, Ni–NTA unbound; E, Ni–NTA eluate. (**b**) Elution profile of the complex from a Superdex 200 column. (**c**,**d**) Negative-stain electron micrographs of the complex (as shown in **b** at 7 ml) between His-GFP-caspase-1^{CARD} and biotinylated ICEBERG after Ni–NTA–gold labeling (**c**) or streptavidin–gold labeling (**d**).

formation of caspase-1^{CARD} filaments by capping small caspase-1^{CARD}-containing nucleators.

To test this hypothesis, we performed gel-filtration analysis to investigate whether His-MBP-caspase-1^{CARD}-SUMO formed complexes with INCA. We incubated caspase-1^{CARD}, at a concentration equivalent to that in the FP assays, with TEV for 90 min at room temperature to remove the N-terminal His-MBP in the presence or absence of a slightly suprastoichiometric amount of INCA. We expected caspase-1^{CARD}-SUMO to remain mostly monomeric in the absence of a nucleator (as in **Fig. 4a**). Upon completion of the polymerization reaction, we injected the mixtures of MBP-cleaved caspase-1 and INCA onto a Superdex 200 column to determine whether a stable complex had formed. No apparent shift in the elution position was present when we ran the two proteins individually or as a mixture (**Supplementary Fig. 5**). This result suggests that INCA does not form a stable complex with caspase-1^{CARD} and consequently sequester the monomeric form but instead caps the oligomeric form.

ICEBERG interacts with caspase-1^{CARD} filaments

To test whether ICEBERG directly interacts with caspase-1^{CARD}, we used a similar strategy as used for INCA and coexpressed biotinylated ICEBERG and His-GFP-caspase-1^{CARD}. Ni–NTA pulldown showed copurified biotinylated ICEBERG, although in an amount substoichiometric to His-GFP-caspase-1^{CARD}, as confirmed by streptavidin western blotting (**Fig. 6a**). In size-exclusion chromatography, the complex eluted in the void fraction (**Fig. 6b**). We labeled the complex with Ni–NTA–gold and streptavidin–gold conjugates separately and subjected it to negative-stain EM analysis to probe the locations of the two proteins in the complex (**Fig. 6c**,**d**). The labeling results showed that both gold conjugates randomly labeled the body of the filaments, indicating that ICEBERG copolymerized with caspase-1^{CARD} into

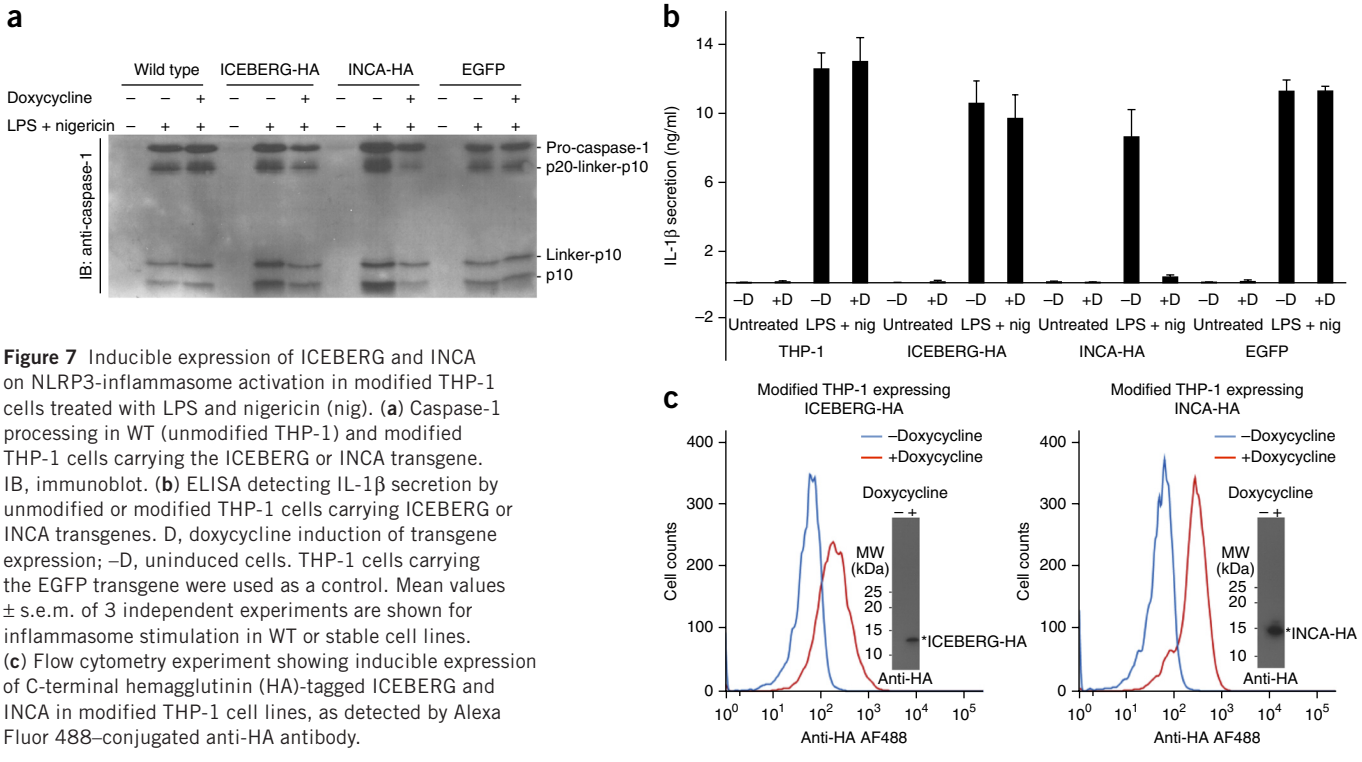

Figure 7 Inducible expression of ICEBERG and INCA on NLRP3-inflammasome activation in modified THP-1 cells treated with LPS and nigericin (nig). (**a**) Caspase-1 processing in WT (unmodified THP-1) and modified THP-1 cells carrying the ICEBERG or INCA transgene. IB, immunoblot. (**b**) ELISA detecting IL-1β secretion by unmodified or modified THP-1 cells carrying ICEBERG or INCA transgenes. D, doxycycline induction of transgene expression; –D, uninduced cells. THP-1 cells carrying the EGFP transgene were used as a control. Mean values ± s.e.m. of 3 independent experiments are shown for inflammasome stimulation in WT or stable cell lines. (**c**) Flow cytometry experiment showing inducible expression of C-terminal hemagglutinin (HA)-tagged ICEBERG and INCA in modified THP-1 cell lines, as detected by Alexa Fluor 488–conjugated anti-HA antibody.

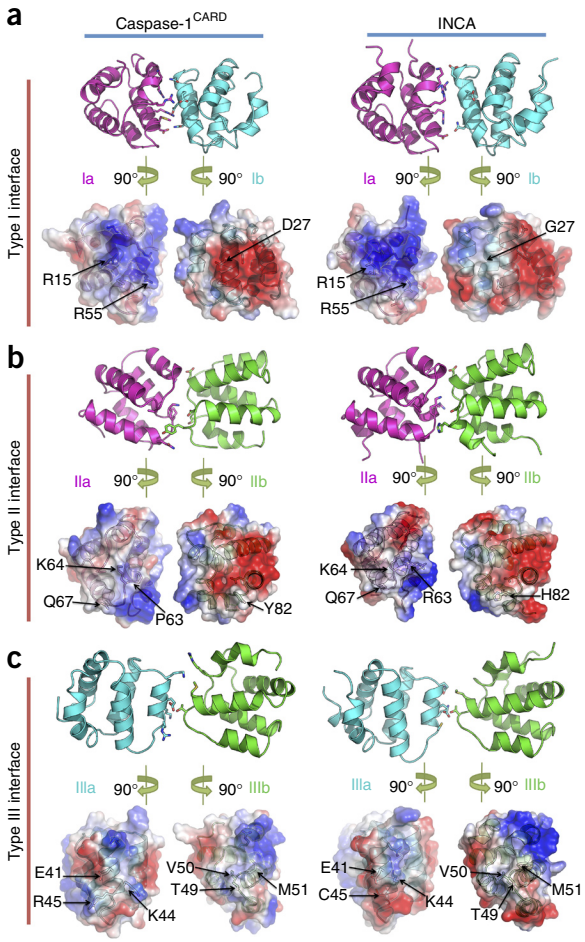

Figure 8 Comparison of critical interface residues between caspase-1^{CARD} and INCA. Model of an INCA monomer generated from the ICEBERG NMR structure as template (PDB 1DGN), superimposed on each subunit in the caspase-1^{CARD}-filament cryo-EM structure by Dali pairwise structural alignment. (**a**–**c**) Type I (**a**), II (**b**), and III (**c**) interfaces of caspase-1^{CARD} and INCA, compared side by side. Each of the colors (magenta, cyan, or green) indicates the same subunit across the three interface types. Electrostatic surface representations of the interfaces are shown with critical residues indicated for comparison.

filaments. Therefore, although both INCA and ICEBERG have been described as CARD-only proteins, INCA clearly functions through a mechanism different from that of ICEBERG.

INCA inhibits NLRP3-inflammasome activation in THP-1 cells

Caspase-1 processing and IL-1β secretion are hallmarks of inflammasome activation. We assayed both to monitor the effect of inducible expression of ICEBERG or INCA in THP-1 cells under physiological conditions (**Fig. 7**). We generated THP-1 cell lines expressing either INCA or ICEBERG and induced expression of the transgenes by the addition of doxycycline for 24 h before the experiments. Importantly, we withdrew doxycycline before inflammasome activation because we noticed that expression of any transgene during inflammasome activation impaired IL-1β secretion (data not shown). We then treated cells for 3 h with LPS and for 45 min with nigericin to induce NLRP3-inflammasome assembly. We first analyzed the processing of caspase-1 by immunoblotting, which showed that INCA expression efficiently inhibited the appearance of the processed forms, whereas ICEBERG expression had minimal effects (**Fig. 7a**). Consistently with these results, the secretion of IL-1β in WT THP-1 cells and in uninduced cell lines was comparable, as quantified by ELISA (**Fig. 7b**). Expression of INCA efficiently inhibited IL-1β secretion in LPS- and nigericin-treated cells, whereas expression of EGFP did not impair IL-1β secretion. Expression of ICEBERG did not have a substantial effect on IL-1β secretion (**Fig. 7b**).

Therefore, in agreement with our *in vitro* data, the cellular experiments support a model in which INCA efficiently perturbs caspase-1 cleavage and activity, presumably because of the inhibition of caspase-1 polymerization. In contrast, ICEBERG did not appear to inhibit NLRP3-dependent inflammasome activation, caspase-1 oligomerization, and caspase-1 activity. However, the situation in cells is substantially more complex, and it is conceivable that ICEBERG levels are insufficient or that ICEBERG binding to caspase-1^{CARD} is subject to regulation by cellular proteins. The question of whether ICEBERG is a genuine inflammasome inhibitor remains to be answered. Even though it physically interacts with caspase-1, the exact molecular mechanism of regulation is unclear.

Structural mechanism of caspase-1 inhibition by INCA

The tendency of DD-fold family proteins to oligomerize into helical oligomers has been extensively demonstrated. Examples of DD helical structures include the PIDDosome (DD)[25], Myddosome (DD)[24], ASC filament (PYD)[5], and MAVS filament (CARD)[22]. To our knowledge, ours is the first reported CARD-filament structure in the inflammasome pathway. For INCA to interact with caspase-1, we predict that it must use CARD-CARD interaction surfaces similar to those observed in the caspase-1^{CARD} filament structure. Hence, we superimposed a predicted INCA monomer model based on the NMR structure of ICEBERG onto the caspase-1^{CARD} filament structure, to visualize the subtle differences between INCA and caspase-1^{CARD} underlying INCA's inhibitory mechanism (**Fig. 8** and **Supplementary Fig. 6**).

For the type I interaction, INCA has a highly similar type Ia interface, marked by the conserved R15 and R55 between caspase-1 and INCA. Strikingly, Asp27 on the caspase-1 type Ib surface has changed to Gly27 in INCA (**Fig. 8a**). This change probably renders the type Ib interface in INCA defective for interaction. According to our mutagenesis studies on caspase-1, type Ib mutation (D27R E28R) completely disrupted filament formation and resulted in the monomeric form of caspase-1 (**Fig. 2h**). The type II interface is primarily hydrophobic in caspase-1, which relies on Tyr82 for the interaction (**Fig. 2f**,**h**). The corresponding position in INCA has changed to His82 (**Fig. 8b**), which probably renders its type IIb interface defective for interaction. The type III interface represents the least extensive interface and is mostly conserved between INCA and caspase-1^{CARD} (**Fig. 8c**).

As a result, we propose a model of how INCA inhibits caspase-1^{CARD} via a capping mechanism, based on the defective type Ib and IIb interfaces, and the intact type Ia, IIa, IIIa, and IIIb interfaces (**Supplementary Fig. 6**). During inflammasome activation by filament formation, and in the absence of the inhibitory protein INCA, oligomerized ASC^{CARD} domains seed caspase-1^{CARD} filaments (**Supplementary Fig. 6a**). In contrast, in the presence of INCA, a small caspase-1^{CARD} oligomer can stochastically recruit one or a few subunits of INCA through its intact type Ia, IIa, IIIa, and IIIb patches, thereby capping the growing caspase-1 filament. Owing to the defective type Ib and IIb patches in INCA, the capped filament then loses the ability to further recruit inactive monomeric caspase-1 (**Supplementary Fig. 6b**). This capping mechanism explains the high inhibitory potency of INCA in blocking the formation of caspase-1^{CARD} filaments in our biochemical assay.

To test this model, we generated a charge-reversal mutant, R55E, at the type Ia interface of INCA, and tested its ability to inhibit GFP-caspase-1-nucleated caspase-1^{CARD} filament formation. Type Ia contains basic residues that are essential for forming the electrostatic interactions between neighboring CARDs. Therefore, we expect this mutation in INCA to lower its affinity for the caspase-1^{CARD} oligomer and thereby abolish its ability to cap the growing caspase-1^{CARD} filament. As expected, the R55E mutation substantially reduced the inhibition potency (**Supplementary Fig. 7**). When we increased the concentrations of R55E in the polymerization assay to drive the inhibition, we derived a K_i of ~1.7 μM for R55E, which is ~400-fold higher than that of WT INCA, thus supporting our proposed capping mechanism.

DISCUSSION

An emerging theme in the field of innate immunity involves the discovery of higher-order signalosomes in ligand binding and signal transduction[30]. The inflammasome assemblies, in particular, use a nucleated polymerization mechanism[5]. Through the formation of filaments and elaborate aggregates in the cell, component proteins come together for efficient activation and signal amplification[5,6]. This mechanism has also been observed in the RIG-I pathway[22,31] and the CARMA1–Bcl10–MALT1 pathway[32] and can be further generalized to related DD-fold-containing proteins in other pathways. Extending the initial discovery of INCA as an inhibitor of LPS-induced and caspase-1-dependent IL-1β secretion[1], we investigated its mechanism of inhibition in the context of higher-order inflammasome assemblies. We found that INCA is a highly efficient inhibitor of caspase-1^{CARD} oligomerization, with an apparent K_i in the nanomolar range. We conclude from our biochemical and structural analyses that INCA caps small oligomers of caspase-1^{CARD} through CARD-CARD interactions, thereby preventing the further recruitment of inactive caspase-1 monomers and the elongation of the CARD filaments (**Supplementary Fig. 8**).

For ICEBERG and COP1, unlike INCA, future studies are required to elucidate their functional mechanisms. ICEBERG oligomerizes and commingles with caspase-1. COP1 has two isoforms: a short isoform with CARD only and a longer isoform with an additional ~100 residues at the C-terminal end. COP1^{CARD} differs from caspase-1^{CARD} in only three residues, two of which, H15 and Q37, reside at the predicted filamentous interface (**Fig. 3d**). However, H15 and Q37 are identical in ICEBERG, and therefore these differences should not affect the interaction of COP1 with caspase-1. Hence, like ICEBERG, COP1 may also commingle with caspase-1 filaments. It remains to be determined whether ICEBERG and COP1 are bona fide inflammasome inhibitors, because our cellular assay did not show any inhibition of NLRP3-inflammasome activation by ICEBERG.

Numerous studies have suggested that inflammasomes may represent important therapeutic targets against human diseases. For example, genetic evidence in the inflammasome sensor proteins NLRP3 (172 known disease variants), Pyrin (also known as MEFV; 297 known disease variants), PSTPIP1 (22 known disease variants), and NLRP12 (32 known disease variants) has linked inflammasomes to hereditary periodic fevers, inflammation, and autoimmunity. More importantly, overactivation of inflammasomes is causal for or associated with highly prevalent inflammatory diseases within and outside the immune system[1,3,33], including gout, rheumatoid arthritis, dermatitis, lung fibrosis[34], irritable and inflammatory bowel diseases[35], neuropathic pain, sepsis, obesity, atherosclerosis[36], diabetes[37,38], and gastric carcinoma. Many of these diseases have limited treatment options, particularly those that specifically address the root of the inflammatory response. The capping mechanism by INCA discovered here permits interference of inflammasome assembly at a highly substoichiometric ratio and provides a new potential therapeutic strategy for inhibition of inflammasomes as well as the many other innate immune signaling complexes that use DD-fold domains as the main scaffolding architectures.

Our work also reveals an unexpected mechanistic connection to capping proteins that dynamically regulate cellular cytoskeletal networks. For instance, the dimeric protein CapZ seals the barbed end of actin filaments, thereby preventing their elongation[39–41]. Human CapZ has a K_{app} of ~3 nM in actin elongation and depolymerization assays[41]. This value is comparable to that of INCA in our caspase-1 polymerization assay. Fungal metabolites known as cytochalasins, which bind actin filaments and block their polymerization, are another example[42]. The effective concentrations of these molecules can range between hundreds of picomolar to several micromolar in cells[43]. The apparent equilibrium dissociation constant of cytochalasin D for ADP–actin is ~1–2 nM (ref. 44). Collectively, our findings suggest that INCA may well be the equivalent of the CapZ or cytochalasin inhibitors in caspase-1 filament elongation, and they illustrate a potential new therapeutic mechanism for inflammasome-associated diseases.

METHODS

Methods and any associated references are available in the online version of the paper.

Accession codes. The EM map of the caspase-1^{CARD} filament has been deposited in the Electron Microscopy Data Bank under accession code EMD-3241. The structure of caspase-1^{CARD} has been deposited in the Protein Data Bank under accession code PDB 5FNA.

Note: Any Supplementary Information and Source Data files are available in the online version of the paper.

ACKNOWLEDGMENTS

The work was supported by US National Institutes of Health (NIH) grants to H.W. (Pioneer Award DP1-HD-087988), to H.L.P. (Pioneer Award DP1-GM-106409), and to Q.Y. (R00: 4R00AI108793-02). F.I.S. was supported by an Advanced Postdoc. Mobility Fellowship from the Swiss National Science Foundation. The cryo-EM facility was funded through the NIH grant AI100645, Center for HIV/AIDS Vaccine Immunology and Immunogen Design (CHAVI-ID). The experiments were performed in part at the Center for Nanoscale Systems at Harvard University, a member of the National Nanotechnology Infrastructure Network (NNIN), which is supported by the US National Science Foundation (NSF) under award no. ECS-0335765. We thank E. Egelman for generous guidance in methods of helical reconstruction.

AUTHOR CONTRIBUTIONS

A.L., Y.L., F.I.S., Q.Y., S.C., T.-M.F., and Y.M. performed the experiments and analyzed the data. A.L., Q.Y., and T.-M.F. purified the recombinant proteins and performed biochemical experiments. S.C. and Y.M. collected the cryo-EM data, and Y.L. processed the data and completed the helical reconstruction. F.I.S. generated stable cell lines and performed cellular assays, and H.L.P. supervised the experiments. A.B.T. performed Rosetta refinement. A.L. and H.W. conceived the study and wrote the manuscript.

COMPETING FINANCIAL INTERESTS

The authors declare no competing financial interests.

1. Lamkanfi, M. & Dixit, V.M. Mechanisms and functions of inflammasomes. *Cell* **157**, 1013–1022 (2014).
2. Latz, E., Xiao, T.S. & Stutz, A. Activation and regulation of the inflammasomes. *Nat. Rev. Immunol.* **13**, 397–411 (2013).
3. Martinon, F., Mayor, A. & Tschopp, J. The inflammasomes: guardians of the body. *Annu. Rev. Immunol.* **27**, 229–265 (2009).
4. Ferrao, R. & Wu, H. Helical assembly in the death domain (DD) superfamily. *Curr. Opin. Struct. Biol.* **22**, 241–247 (2012).

5. Lu, A. *et al.* Unified polymerization mechanism for the assembly of ASC-dependent inflammasomes. *Cell* **156**, 1193–1206 (2014).
6. Cai, X. *et al.* Prion-like polymerization underlies signal transduction in antiviral immune defense and inflammasome activation. *Cell* **156**, 1207–1222 (2014).
7. Zhang, L. *et al.* Cryo-EM structure of the activated NAIP2-NLRC4 inflammasome reveals nucleated polymerization. *Science* **350**, 404–409 (2015).
8. Hu, Z. *et al.* Structural and biochemical basis for induced self-propagation of NLRC4. *Science* **350**, 399–404 (2015).
9. Qu, Y. *et al.* Phosphorylation of NLRC4 is critical for inflammasome activation. *Nature* **490**, 539–542 (2012).
10. Kofoed, E.M. & Vance, R.E. Innate immune recognition of bacterial ligands by NAIPs determines inflammasome specificity. *Nature* **477**, 592–595 (2011).
11. Vezzani, A., Maroso, M., Balosso, S., Sanchez, M.A. & Bartfai, T. IL-1 receptor/Toll-like receptor signaling in infection, inflammation, stress and neurodegeneration couples hyperexcitability and seizures. *Brain Behav. Immun.* **25**, 1281–1289 (2011).
12. Stehlik, C. *et al.* The PAAD/PYRIN-only protein POP1/ASC2 is a modulator of ASC-mediated nuclear-factor-kappa B and pro-caspase-1 regulation. *Biochem. J.* **373**, 101–113 (2003).
13. Bedoya, F., Sandler, L.L. & Harton, J.A. Pyrin-only protein 2 modulates NF-kappaB and disrupts ASC:CLR interactions. *J. Immunol.* **178**, 3837–3845 (2007).
14. Dorfleutner, A. *et al.* A Shope Fibroma virus PYRIN-only protein modulates the host immune response. *Virus Genes* **35**, 685–694 (2007).
15. Lamkanfi, M. *et al.* INCA, a novel human caspase recruitment domain protein that inhibits interleukin-1beta generation. *J. Biol. Chem.* **279**, 51729–51738 (2004).
16. Humke, E.W., Shriver, S.K., Starovasnik, M.A., Fairbrother, W.J. & Dixit, V.M. ICEBERG: a novel inhibitor of interleukin-1beta generation. *Cell* **103**, 99–111 (2000).
17. Druilhe, A., Srinivasula, S.M., Razmara, M., Ahmad, M. & Alnemri, E.S. Regulation of IL-1beta generation by Pseudo-ICE and ICEBERG, two dominant negative caspase recruitment domain proteins. *Cell Death Differ.* **8**, 649–657 (2001).
18. Le, H.T. & Harton, J.A. Pyrin- and CARD-only proteins as regulators of NLR functions. *Front. Immunol.* **4**, 275 (2013).
19. Kersse, K., Vanden Berghe, T., Lamkanfi, M. & Vandenabeele, P. A phylogenetic and functional overview of inflammatory caspases and caspase-1-related CARD-only proteins. *Biochem. Soc. Trans.* **35**, 1508–1511 (2007).
20. Lee, S.H., Stehlik, C. & Reed, J.C. Cop, a caspase recruitment domain-containing protein and inhibitor of caspase-1 activation processing. *J. Biol. Chem.* **276**, 34495–34500 (2001).
21. da Cunha, J.P., Galante, P.A. & de Souza, S.J. Different evolutionary strategies for the origin of caspase-1 inhibitors. *J. Mol. Evol.* **66**, 591–597 (2008).
22. Wu, B. *et al.* Molecular imprinting as a signal-activation mechanism of the viral RNA sensor RIG-I. *Mol. Cell* **55**, 511–523 (2014).
23. Egelman, E.H. The iterative helical real space reconstruction method: surmounting the problems posed by real polymers. *J. Struct. Biol.* **157**, 83–94 (2007).
24. Lin, S.C., Lo, Y.C. & Wu, H. Helical assembly in the MyD88–IRAK4–IRAK2 complex in TLR/IL-1R signalling. *Nature* **465**, 885–890 (2010).
25. Park, H.H. *et al.* Death domain assembly mechanism revealed by crystal structure of the oligomeric PIDDosome core complex. *Cell* **128**, 533–546 (2007).
26. Lu, A. *et al.* Plasticity in PYD assembly revealed by cryo-EM structure of the PYD filament of AIM2. *Cell Discov.* **1**, 15013 (2015).
27. Guimaraes, C.P. *et al.* Site-specific C-terminal and internal loop labeling of proteins using sortase-mediated reactions. *Nat. Protoc.* **8**, 1787–1799 (2013).
28. de Alba, E. Structure and interdomain dynamics of apoptosis-associated speck-like protein containing a CARD (ASC). *J. Biol. Chem.* **284**, 32932–32941 (2009).
29. Tsao, K.L., DeBarbieri, B., Michel, H. & Waugh, D.S. A versatile plasmid expression vector for the production of biotinylated proteins by site-specific, enzymatic modification in *Escherichia coli*. *Gene* **169**, 59–64 (1996).
30. Wu, H. Higher-order assemblies in a new paradigm of signal transduction. *Cell* **153**, 287–292 (2013).
31. Hou, F. *et al.* MAVS forms functional prion-like aggregates to activate and propagate antiviral innate immune response. *Cell* **146**, 448–461 (2011).
32. Qiao, Q. *et al.* Structural architecture of the CARMA1/Bcl10/MALT1 signalosome: nucleation-induced filamentous assembly. *Mol. Cell* **51**, 766–779 (2013).
33. López-Castejón, G. & Pelegrín, P. Current status of inflammasome blockers as anti-inflammatory drugs. *Expert Opin. Investig. Drugs* **21**, 995–1007 (2012).
34. Brusselle, G.G., Provoost, S., Bracke, K.R., Kuchmiy, A. & Lamkanfi, M. Inflammasomes in respiratory disease: from bench to bedside. *Chest* **145**, 1121–1133 (2014).
35. Aguilera, M., Darby, T. & Melgar, S. The complex role of inflammasomes in the pathogenesis of inflammatory bowel diseases: lessons learned from experimental models. *Cytokine Growth Factor Rev.* **25**, 715–730 (2014).
36. Ridker, P.M. & Lüscher, T.F. Anti-inflammatory therapies for cardiovascular disease. *Eur. Heart J.* **35**, 1782–1791 (2014).
37. Esser, N., Legrand-Poels, S., Piette, J., Scheen, A.J. & Paquot, N. Inflammation as a link between obesity, metabolic syndrome and type 2 diabetes. *Diabetes Res. Clin. Pract.* **105**, 141–150 (2014).
38. Robbins, G.R., Wen, H. & Ting, J.P. Inflammasomes and metabolic disorders: old genes in modern diseases. *Mol. Cell* **54**, 297–308 (2014).
39. Caldwell, J.E., Heiss, S.G., Mermall, V. & Cooper, J.A. Effects of CapZ, an actin capping protein of muscle, on the polymerization of actin. *Biochemistry* **28**, 8506–8514 (1989).
40. Lin, Y.H., Li, J., Swanson, E.R. & Russell, B. CapZ and actin capping dynamics increase in myocytes after a bout of exercise and abates in hours after stimulation ends. *J. Appl. Physiol. (1985)* **114**, 1603–1609 (2013).
41. Maun, N.A., Speicher, D.W., DiNubile, M.J. & Southwick, F.S. Purification and properties of a Ca^{2+}-independent barbed-end actin filament capping protein, CapZ, from human polymorphonuclear leukocytes. *Biochemistry* **35**, 3518–3524 (1996).
42. Cooper, J.A. Effects of cytochalasin and phalloidin on actin. *J. Cell Biol.* **105**, 1473–1478 (1987).
43. Wakatsuki, T., Schwab, B., Thompson, N.C. & Elson, E.L. Effects of cytochalasin D and latrunculin B on mechanical properties of cells. *J. Cell Sci.* **114**, 1025–1036 (2001).
44. Carlier, M.F., Criquet, P., Pantaloni, D. & Korn, E.D. Interaction of cytochalasin D with actin filaments in the presence of ADP and ATP. *J. Biol. Chem.* **261**, 2041–2050 (1986).

ONLINE METHODS

Protein purification. All proteins were expressed in chemically competent BL21(DE3) *E. coli* cells through overnight induction with 0.4 mM IPTG at 16 °C. Cells expressing hexahistidine (His)-tagged constructs were lysed by sonication in a buffer containing 20 mM sodium HEPES, pH 8.0, 150 mM NaCl, 5 mM imidazole, 10% glycerol, and 5 mM β-mercaptoethanol. Whole cell lysates were centrifuged at 30,000*g* for 40 min. The supernatant was incubated with Ni–NTA resin (Qiagen) for 1 h. The resin was washed with lysis buffer containing 20 mM imidazole. The target proteins were eluted with lysis buffer containing 300 mM imidazole. Subsequent size-exclusion purification or gel-filtration analysis was performed on a Superdex 200 10/300 GL column (GE Healthcare) in a buffer containing 20 mM sodium HEPES, pH 8.0, 150 mM NaCl, and 2 mM DTT. Biotinylated complexes were expressed and purified through the same procedure except for the addition of 50 μM biotin during IPTG induction. The presence of biotin was confirmed by western blotting with streptavidin-conjugated alkaline phosphatase (streptavidin-AP, Molecular Probes, S921).

Cryo-EM data collection. Protein (3 μl) was applied to glow-discharged holey carbon C-flat grids (R1.2/1.3, Photochip), blotted for 3 s, and plunged into liquid ethane in an FEI Vitrobot Mark VI. Frame-packed micrographs were semiautomatically recorded on a FEI Tecnai Arctica Cryo-TEM operating at 200 KeV with a K2 summit direct electron detector, under super-resolution counting mode with a 0.87-Å pixel size. A total of 509 video-mode micrographs were collected. The exposure time was 6 s, and each video stack contained 30 subframes with 200-ms exposure per frame. The accumulated dose in each stack was 20 e^{-}/Å^2.

Cryo-EM reconstruction and structure determination. The helical reconstruction was performed with the iterative helical real-space reconstruction (IHRSR) method[23]. Each subframe was subjected to gain correction and motion correction with SPIDER[45] and then summed to a single image. The defocus range, determined by CTFFIND3 (ref. 46), was from 1 to 6 μm. Images with defocus higher than 5 μm or still containing severe astigmatism were excluded. 69,222 segments were cut out from the remaining images, with a box size of 200 × 384 pixels and an overlap of 374 pixels (97%). The experimental power spectrum was calculated from the original segments that were padded into 1024 × 1024 pixels, with a pixel size of 0.87 Å. For the diffraction lines marked as $n = 2$, $n = -1$, $n = 3$, and $n = -4$, the Y coordinates were 78, 49, 29, and 20 pixels, respectively, and the X coordinates were approximately 11, −7, 16, and −22 pixels. By indexing the power spectrum, an initial helical symmetry of 5.1 Å in rise and −100.2° in rotation per subunit was obtained. Initial reconstruction was carried out with 4 × 4 binned segments, staring from a solid cylinder to avoid any model bias. Further refinement was gradually expanded to the pixel size of the super-resolution mode. Finally, out-of-plane tilt was calculated and imposed on these segments until convergence, leading to the final reconstruction. The final density started to show helical features. To perform gold-standard Fourier-shell correlation (FSC)[47], we split the sorted data set into two independent halves. Two parallel helical reconstructions were executed starting from the solid cylinder model and with the same settings and refinement cycles. The resolution was 4.8 Å, on the basis of an 0.143 cutoff of the gold-standard FSC.

Model building and refinement. The NMR structure of ICEBERG (PDB 1DGN)[16] was uploaded to the Swiss-Model server[48] to generate an initial caspase-1^{CARD} homology model. The initial model was adjusted manually in COOT[49] toward the cryo-EM density. A filament model containing eight caspase-1^{CARD} subunits was generated in UCSF Chimera[50] by applying the helical symmetry. The density corresponding to this filament model was masked in CCP4 (ref. 51) and was Fourier transformed to structure factors in the MTZ format with PHENIX[52]. After rigid-body phased refinement with PHENIX.refine, the structure was further refined in real space with Rosetta[53]. The model-map cross-validation FSC had a value of 0.45 at 4.8-Å resolution.

Sortase labeling and fluorescence polarization assay. Constructs for sortase labeling and polymerization assays contained a C-terminal LPETG polypeptide motif. Calcium-independent sortase- and TAMRA-conjugated triglycine nucleophile (GGG-TAMRA) were used[54]. In brief, 30 μM of a freshly purified protein substrate with the LPETG motif was incubated with 5 μM sortase and 500 μM GGG-TAMRA overnight at 4 °C. The labeled substrate and the excess nucleophile were separated by size-exclusion chromatography. Labeled proteins were diluted to the desired concentrations for FP assays on a SpectraMax M5e plate reader. Traces of polarization values were averaged for triplicate experiments and plotted in Microsoft Excel.

Calculation of apparent dissociation (K_{app}) and inhibitory (K_i) constants. To estimate the apparent dissociation constants between nucleators and polymerizing monomers and the inhibitory constant of INCA, we extracted the slopes of the initial linear phase of the FP traces in units of mP/min and plotted them against the log of the concentrations of the added nucleators or INCA. The profiles were fitted in Prism 6.0 for Windows (GraphPad Software, http://www.graphpad.com/) with three-parameter agonist or antagonist functions to determine the concentration of the nucleator or the inhibitor at the half-maximal effect.

Nanogold labeling and negative-stain electron microscopy. Gel-filtration-purified proteins and protein complexes were embedded on a Formvar carbon-coated EM grid (CFC400-Cu, Electron Microscopy Sciences) and washed three times. The grids were blotted to remove excess sample and incubated upside-down on a drop containing suitable dilution of the Ni–NTA–gold reagent (5 nm, Nanoprobes) or streptavidin–gold reagent (6 nm, Electron Microscopy Sciences). The grids were washed to remove unbound gold and stained with uranyl acetate for negative-stain EM analysis. More detailed protocols of these experiments can be found in the methods of our previous paper[5].

Generation of INCA- and ICEBERG-overexpressing THP-1 cell lines. THP-1 human monocyte-like cells (obtained from ATCC) were cultivated in RPMI with 10% FBS and 50 μM 2-mercaptoethanol. THP-1 cell lines inducibly expressing HA-tagged EGFP, ICEBERG, and INCA were generated with lentivirus produced with derivatives of pInducer20 (ref. 55) and selected in the presence of 500 μg/ml G418. Monoclonal cell lines were obtained by limited dilution in THP-1 medium with 20% FBS. For testing mycoplasma contamination, WT and derived THP-1 cells were stained with Hoechst 33342 and analyzed at high magnification. No punctate DNA staining was observed in the cytosol. Alexa Fluor 488–conjugated anti-HA mouse IgG monoclonal antibody (clone 16B12) from Life Technologies (A21287) was used to confirm ICEBERG-HA and INCA-HA expression in modified THP-1 cells. Anti-HA specificity of the antibody has been tested by the manufacturer.

NLRP3 -inflammasome activation assay. To quantify IL-1β secretion in response to NLRP3 triggers, THP-1 cell lines were seeded into 24-well plates (2.5×10^5 cells per well) and cultivated in the presence of 50 nM phorbol-12-myristate-13-acetate (PMA, Santa Cruz Biotechnology) for 16 h. Cells were then grown in full medium with or without 1 μg/ml doxycycline for 24 h, sensitized in the presence of 200 ng/ml LPS (from *E. coli* K12, InvivoGen) for 3 h, and treated with 5 μM nigericin in 0.5 ml OptiMEM per well for 45 min. Control samples were incubated with medium lacking LPS or nigericin. Supernatants were harvested, cell debris was removed by a 10-min spin (1000*g*, 4 °C), and samples were stored at −20 °C. IL-1β levels in a 1:200 dilution of the supernatant were determined with a BD OptEIA Human IL-1β ELISA Set II (BD Biosciences) according to the manufacturer's instructions.

Homology modeling of INCA. A monomeric model of INCA was generated with the online Swiss-Model server[48] with the ICEBERG NMR structure (PDB 1DGN[16]) as the template. The INCA model was aligned to each subunit of the caspase-1^{CARD}-filament cryo-EM structure with the Dali structural alignment server to generate an oligomeric INCA model[56]. Cartoon representations and surface electrostatic potential maps were generated in PyMOL (http://www.pymol.org/).

45. Shaikh, T.R. *et al.* SPIDER image processing for single-particle reconstruction of biological macromolecules from electron micrographs. *Nat. Protoc.* **3**, 1941–1974 (2008).
46. Mindell, J.A. & Grigorieff, N. Accurate determination of local defocus and specimen tilt in electron microscopy. *J. Struct. Biol.* **142**, 334–347 (2003).

doi:10.1038/nsmb.3199

47. Scheres, S.H. & Chen, S. Prevention of overfitting in cryo-EM structure determination. *Nat. Methods* **9**, 853–854 (2012).
48. Biasini, M. *et al.* SWISS-MODEL: modelling protein tertiary and quaternary structure using evolutionary information. *Nucleic Acids Res.* **42**, W252–W258 (2014).
49. Emsley, P. & Cowtan, K. Coot: model-building tools for molecular graphics. *Acta Crystallogr. D Biol. Crystallogr.* **60**, 2126–2132 (2004).
50. Pettersen, E.F. *et al.* UCSF Chimera: a visualization system for exploratory research and analysis. *J. Comput. Chem.* **25**, 1605–1612 (2004).
51. Winn, M.D. *et al.* Overview of the CCP4 suite and current developments. *Acta Crystallogr. D Biol. Crystallogr.* **67**, 235–242 (2011).
52. Adams, P.D. *et al.* PHENIX: a comprehensive Python-based system for macromolecular structure solution. *Acta Crystallogr. D Biol. Crystallogr.* **66**, 213–221 (2010).
53. DiMaio, F. *et al.* Atomic-accuracy models from 4.5-Å cryo-electron microscopy data with density-guided iterative local refinement. *Nat. Methods* **12**, 361–365 (2015).
54. Hirakawa, H., Ishikawa, S. & Nagamune, T. Design of Ca^{2+}-independent *Staphylococcus aureus* sortase A mutants. *Biotechnol. Bioeng.* **109**, 2955–2961 (2012).
55. Meerbrey, K.L. *et al.* The pINDUCER lentiviral toolkit for inducible RNA interference *in vitro* and *in vivo*. *Proc. Natl. Acad. Sci. USA* **108**, 3665–3670 (2011).
56. Holm, L. & Sander, C. Dali: a network tool for protein structure comparison. *Trends Biochem. Sci.* **20**, 478–480 (1995).